

Quantum rotation of $\text{Rb}_2(^3\Sigma_u^+)$ attached to He_N droplets: A path-integral Monte Carlo study

R. Rodríguez-Cantano^{1a}, R. Pérez de Tudela², D. López-Durán³, T. González-Lezana¹, F. A. Gianturco⁴, G. Delgado-Barrio¹ and P. Villarreal¹

¹ Inst. de Física Fundamental (CSIC), Serrano 123, 28006 Madrid, Spain;

² Dep. de Química-Física I, Universidad Complutense de Madrid, Avda. Complutense s/n, 28040 Madrid, Spain

³ Inst. de Catálisis y Petroleoquímica - CSIC, Marie Curie 2, Cantoblanco, 28049 Madrid, Spain

⁴ Dep. of Chemistry, University of Rome La Sapienza, Piazzale A. Moro 5, 00185 Rome, Italy

April 26, 2013; to submit to EPJD

Abstract. Doped $\text{He}_N\text{Rb}_2(^3\Sigma_u^+)$ systems, with $N = 20$ and 40 , have been studied by means of a path integral Monte Carlo method at two different temperatures $T = 1$ K and 2 K. The impurity, Rb_2 , is assumed as a rigid rotor and results are compared with a previous analysis in which no rotational or translational degrees of freedom were taken into account. Quantum effects are observed to play a noticeable role accounting for the extra energy with respect to the fixed Rb_2 case although differences between the two approaches do not seem to be as important as reported for some other dopants attached to helium droplets, such as OCS for example. Probability density distributions exhibit the same overall features as the non-rotating system, predicting the outer location of Rb_2 with respect to the helium atoms. The stability of the two clusters under study at $T = 2$ K is uncertain: the energy of $\text{He}_{20}\text{Rb}_2$ is positive and for $\text{He}_{40}\text{Rb}_2$, the observed dependence on the confinements imposed on the system precludes definitive statements regarding its physical existence.

PACS. 36.40.-c Atomic and molecular clusters

1 Introduction

Motivated by their unique properties as an ideal matrix to perform spectroscopic measurements at low temperature, helium nanodroplets have been the subject of numerous theoretical works in the last decades. In particular path integral Monte Carlo (PIMC) simulations have investigated solvated rotating impurities such as N_2O [1–4], HCCH [5], HCCCN [6], OCS [5,7,8] or CO_2 [2,9,10] embedded in He_N clusters in order to explore superfluidity effects as a function of the cluster size N at $T < 1$ K. Within the large diversity of possible impurities, alkali dimers have also received a great deal of interest. A wide variety of methods ranging between diffusion Monte Carlo (DMC) [11–15], quantum dynamical calculations [16–19], variational [13], PIMC treatments [20–22] or density functional formalism [23] have been applied to investigate structural and dynamical properties of these $\text{He}_N\text{-X}$ systems. Previous experimental investigations have observed a preference for the alkali diatom to locate along the surface of the nanodroplet [24–30], an expected result due the usually weak interactions between the corresponding dopant and the helium atoms. In those cases in which the difference with respect to the mass of the He atom is sufficiently large,

X is assumed to have an infinite mass and to remain in a fixed position [31–33] within the cluster. Analogously, and given that nuclear effects of intramolecular vibrations are negligible at low temperature [34], the diatom can be considered as a linear rigid rotor [35]. This constituted a working assumption in previously reported studies [36] on the $\text{He}_N\text{-Rb}_2$ cluster considered here.

Rigid Rb_2 dimers attached to small He_N droplets, $N \leq 4$, have been the subject of DMC and quantum variational investigations on a new full-dimension *ab initio* potential energy surface of $\text{He-Rb}_2(^3\Sigma_u^+)$ [15]. DMC calculations for larger clusters, $N \leq 20$, revealed that the Rb_2 molecule remains bound outside the He_N cluster [37]. The stability between $1 \text{ K} \leq T \leq 2 \text{ K}$ for aggregates up to $N = 40$ was studied by means of a PIMC method in which the Rb_2 was assumed to be fixed at the origin with no translational or rotational movements [22]. $\text{He}_N\text{-Rb}_2$ systems were found to exhibit a trend to higher stabilization as the number of He atoms, N , increases. Guillon *et al.* [21] developed a different potential for a rigid $\text{Rb}_2(^3\Sigma_u^+)$ interacting with a He atom and performed quantum Monte Carlo (MC) calculations for both $\text{He}_N\text{-Rb}_2$ clusters with $N \leq 20$ and for Rb_2 on a He surface. Directly related with this subject, collisions between He and Rb_2 have been investigated by means of quantum mechanical scattering calculations

^a Corresponding author: Email: rrcantano@iff.csic.es

on a new surface for the system in which the internal vibrational degrees of freedom of the rubidium diatom have been included [38].

In this work we perform PIMC calculations on the He_N-Rb₂(³Σ_u⁺) clusters for $N = 20$ and 40 and $T \geq 1$ K including translational and rotational degrees of freedom of the Rb₂ impurity, thus extending our previous investigation on the title system [22]. Similarly to references [22,33], exchange effects are excluded, a reasonable assumption for the cluster sizes at the range of temperature considered here [31]. Furthermore, the present study broadens both the temperature range and the size of the helium nanodroplets considered in Ref. [21].

This paper is organized as follows: Section 2 presents a brief description of the PIMC methodology including both rotational and translational degrees of freedom of a doped cluster. In Section 3 and 4 we report simulation details of our calculations and the results including impurity rotation in comparison to previous non-rotating dopant. Finally, Section 5 illustrates our main conclusions.

2 Theory

Over the past years, the PIMC method has become one of the most powerful computational tool for the microscopic description of the many-body quantum system at finite temperature. A detailed review of this methodology is given in references [39,40], but we will provide in this section the requirements imposed on the PIMC algorithm by the system of interest.

The total Hamiltonian \hat{H} can be considered as [32,41]:

$$\hat{H} = \hat{V}^{pot} + \hat{K}^{kin} + \hat{K}_{imp}^{rot} \quad (1)$$

The potential energy \hat{V}^{pot} includes the He-He and He-dimer interactions:

$$\hat{V}^{pot} = \sum_{i < j}^N V_{\text{He}_i - \text{He}_j} + \sum_{i=1}^N V_{\text{He}_i - \text{imp}} \quad (2)$$

Kinetic part of the hamiltonian includes the helium and impurity translational degrees of freedom:

$$\hat{K}^{kin} = -\frac{\hbar^2}{2m_{\text{He}}} \sum_{i=1}^N \nabla_i^2 - \frac{\hbar^2}{2m_{\text{imp}}} \nabla_{\text{imp}}^2 \quad (3)$$

with m_{He} the mass of a helium atom and m_{imp} the total mass of the Rb₂ molecule.

Finally, \hat{K}_{imp}^{rot} represents the rotational kinetic energy operator given by:

$$\hat{K}_{imp}^{rot} = B\hat{L}^2 \quad (4)$$

where \hat{L} is the rotational molecule angular momentum and B its rotational constant.

Through the PIMC approach, one is interested in computing the thermal average of a quantum observable \hat{A} at a given temperature T in function of the density matrix of the system,

$$\rho(R, R'; \beta) = \langle R | e^{-\beta \hat{H}} | R' \rangle, \quad (5)$$

via the expression:

$$\langle \hat{A} \rangle = \frac{1}{Z} \int dR dR' \langle R | \hat{A} | R' \rangle \times \rho(R, R'; \beta), \quad (6)$$

where $\beta = 1/k_B T$, $Z = \int dR \rho(R, R; \beta)$ is the partition function and R is a vector which contains translational (\mathbf{R}) and rotational ($\mathbf{\Omega}$) degrees of freedom of the system. In particular, $\mathbf{R} = (\mathbf{r}_0, \mathbf{r}_1, \mathbf{r}_2, \dots, \mathbf{r}_N)$, with \mathbf{r}_0 the position of the impurity center of mass (CM) and \mathbf{r}_i the vector position of the i -th helium atom, and $\mathbf{\Omega}$ a set of Euler angles in the laboratory frame [32,42], that fix the impurity orientation.

The full density matrix in Eq.(5) at T , is splitted into the product of M higher temperature density matrices:

$$\rho(R, R'; \beta) = \int dR^1 \dots dR^{M-1} \rho(R, R^1; \tau) \dots \times \rho(R^t, R^{t+1}; \tau) \dots \rho(R^{M-1}, R'; \tau) \quad (7)$$

where R^t is the previously defined vector R at the time slice t and M is the number of beads which constitutes each quantum path [43]. At a sufficiently small $\tau = \beta/M$, the density matrix $\rho(R^t, R^{t+1}; \tau) = e^{-\tau \hat{H}}$ can be approximated by a high temperature expansion [44]. Using the *primitive* approximation [45] and as a result of the additive structure of the Hamiltonian given in Eq.(1), the high-temperature density matrix can be factorized into three components:

$$\rho(R^t, R^{t+1}; \tau) \approx \langle \mathbf{R}^t \mathbf{\Omega}^t | e^{-\tau \hat{V}/2} e^{-\tau (\hat{K}^{kin} + \hat{K}^{rot})/2} \times e^{-\tau \hat{V}/2} | \mathbf{R}^{t+1} \mathbf{\Omega}^{t+1} \rangle \quad (8)$$

Because \hat{V} is diagonal in coordinate space and because \hat{K}^{kin} and \hat{K}^{rot} commute in the rigid-rotor approximation, one obtains [40]:

$$\rho(R^t, R^{t+1}; \tau) \approx \rho_{pot}^{t,t+1} \rho_{kin}^{t,t+1} \rho_{rot}^{t,t+1} \quad (9)$$

with

$$\rho_{pot}(R^t, R^{t+1}; \tau) = \exp \left[-\frac{\tau}{2} (V(R^t) + V(R^{t+1})) \right] \quad (10)$$

and

$$\begin{aligned} \rho_{kin}(\mathbf{R}^t, \mathbf{R}^{t+1}; \tau) &= \left(\frac{m_{\text{He}}}{2\pi\tau} \right)^{3N/2} \left(\frac{m_{\text{imp}}}{2\pi\tau} \right)^{3/2} \\ &\times \exp \left[-\frac{m_{\text{imp}}}{2\hbar^2\tau} (\mathbf{r}_0^t - \mathbf{r}_0^{t+1})^2 \right] \\ &\times \exp \left[-\sum_{i=1}^N \frac{m_{\text{He}}}{2\hbar^2\tau} (\mathbf{r}_i^t - \mathbf{r}_i^{t+1})^2 \right] \end{aligned} \quad (11)$$

In order to obtain the rotational propagator in the linear rigid rotor approximation, we have particularised the general expression of Ref. [42] for rigid tops for the case of a symmetric linear molecule. Thus, the rotational contribution to the propagator between *beads* t and $t+1$ depends on the relative angle θ formed by both symmetry axis. It is exactly given by [32, 40, 46] :

$$\rho_{rot}^{t,t+1}(\Omega^t, \Omega^{t+1}; \tau) = \sum_{l=0}^{\infty} \frac{2l+1}{4\pi} P_l(\cos \theta) e^{-\tau B l(l+1)} \quad (12)$$

where P_l is the Legendre polynomial with l the impurity angular momentum.

Once the three contributions to the density function, see Eq. (9), have been obtained, we can calculate the partition function of the system and therefore any physical property of the cluster. The present study includes energy values computed using the estimators proposed by [35] for rotational and potential energy, and by references [47, 48] for the kinetic one. More specifically, the functional forms used for these three components are:

$$E_{pot} = \left\langle \frac{1}{M} \sum_{t=1}^M V(R^t) \right\rangle \quad (13)$$

$$E_{kin} = \frac{3N}{2\beta} + \left\langle \frac{1}{2M} \sum_{i=0}^N \sum_{t=1}^M (\mathbf{r}_i^t - \mathbf{r}_i^{CM}) \frac{\partial V(\mathbf{r}_i^t)}{\partial \mathbf{r}_i^t} \right\rangle \quad (14)$$

$$E_{rot} = \left\langle \frac{1}{M} \sum_{t=1}^M [\rho_{rot,i}^{t,t+1}]^{-1} \times \sum_{l=0}^{\infty} \frac{2l+1}{4\pi} E_l P_l(\cos \theta) e^{-\tau E_l} \right\rangle \quad (15)$$

with $E_l = Bl(l+1)$ and $\mathbf{r}_i^{cm} = \sum_{t=1}^M \mathbf{r}_i^t / M$. The contribution from the total CM has been substracted in Eq.(14) for the classical kinetic energy.

It is worth mentioning that the orientational propagator, $\rho_{rot}^{t,t+1}$, must be positive, as required by the Metropolis acceptance criteria [49] during the sampling process. In order to fulfill this assumption we have restricted rotation sampling to orientation between contiguous *beads* to angles confined in the range of 0 to the first nodal point of the orientational propagator (See Fig.1). To clarify the imposed constraint, we can define a potential function $u_{rot}^{t,t+1}$ using (7): $u_{rot}^{t,t+1} = -\beta^{-1} \log(\rho_{rot}^{t,t+1})$, referred by several authors as an effective [7] or auxiliary [50] potential of quantum rotation. Therefore, the role of the orientational propagator may be viewed as a potential that forces *beads* t and $t+1$ to adopt similar orientations (minimum of $u_{rot}^{t,t+1}$ function corresponds to $\theta \rightarrow 0$, Fig.1). Moreover, given the definition of the effective potential, one can easily see that if $\rho_{rot}^{t,t+1}$ gets negative values, then $u_{rot}^{t,t+1}$ diverges, avoiding sampling angles greater than that for which $\rho_{rot}^{t,t+1} < 0$.

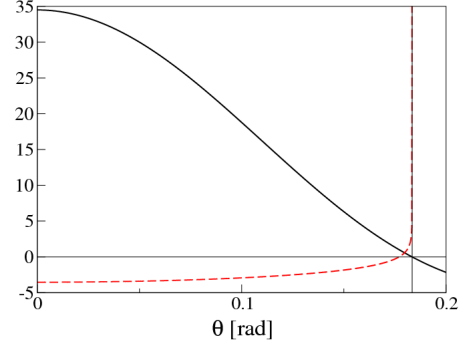


Fig. 1. Example of unnormalized rotational density matrix $\rho_{rot}^{t,t+1}$ Eq.(5) (black line) and $u_{rot}^{t,t+1}$ (red dashed line) for $M = 180$, $T = 1$ K, $l = 20$ and $B = 9.8 \times 10^{-3} \text{ cm}^{-1}$.

3 Simulation details

In this work simulations are undertaken for He_N-Rb₂ clusters with $N = 20$ and 40 at temperatures of 1 and 2 K. For this purpose the Rb₂ dimer is treated as a linear rigid rotor with a total mass of $m_{imp} = 170.9356$ (amu), a rotational constant value of $9.8 \times 10^{-3} \text{ cm}^{-1}$ [15] and a Rb₂ distance equal to 6.35 \AA . In order to estimate the value of a specific observable at a given temperature, Eq. (6), around $10^7 - 10^8$ MC steps have been carried out after a thermalization process. The sampling procedure is performed by the Metropolis algorithm [49] both for rotational and translational degrees of freedom. In the latter, the staging method [51] is also applied. The widely used form of Aziz potential [52] is employed as pairwise interaction between two helium atoms. For the $V_{\text{He-Rb}_2}$ term the analytical form proposed by [15] was adopted. To obtain accurate total energy values, a convergence study with respect to the numbers of *beads* was carried out. In the present calculations we used M around 250 for the high-temperature density matrix. This has been sufficient to obtain converged energy results.

As consequence of the weak interactions that come into play, the PIMC calculations have been executed with two artificial constraints preventing the helium atoms from undergoing evaporation : they are confined inside a sphere centered at the diatomic CM with a radius of 30 \AA , and they are not allowed to exceed a maximum distance of 15 \AA from the CM of the helium drop.

The simulations for each cluster size were started from the lowest classical potential energy structure, which corresponds to a T-shape configuration of -582.66 cm^{-1} and -1321.06 cm^{-1} for He₂₀-Rb₂ and He₄₀-Rb₂ respectively. These arrangements were obtained by a standard evolutionary algorithm [53] and are shown in Fig.2 .

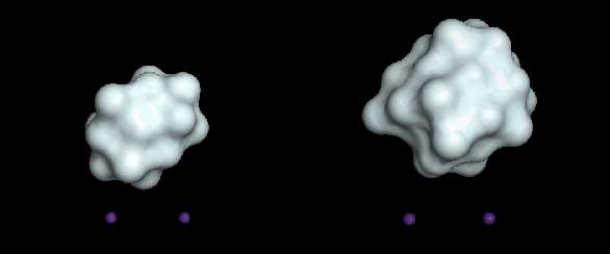


Fig. 2. Initial geometries for $N = 20$ (left) and $N = 40$ (right) clusters.

4 Results and Discussion

4.1 Energetics

The energetics of $\text{He}_N\text{-Rb}_2$ clusters, with sizes varying from 20 to 40 at $T = 1$ K and 2 K obtained by means of the PIMC method and discussed in the previous sections, are summarized in Table 1. Besides the total energy, E , the separate contributions coming from the potential, E_{pot} , the kinetic, E_{kin} , and the rotational, E_{rot} , terms are presented. All energies correspond to a sufficiently large value of M within the region $E = E(M)$ in which the convergence is ensured. We also include results obtained within the framework adopted in Ref. [22] with regard to the treatment for the Rb_2 impurity, that is, an infinite mass ($m_{\text{imp}} \gg m_{\text{He}}$) which leads to neglect translational and rotational movements and to a classical approach, in which the number of *beads* dedicated to describe the Rb atoms is restricted to 1. A similar comparison between a quantum and a fixed impurity framework has been established before in a study of $\text{He}_N\text{-OCS}$ for example [7].

It is worth noticing that values of the total energy E shown in Table 1 for the fixed Rb_2 for $N = 20$ and 40 at the two temperatures under consideration still differ from those reported in Ref. [22]. There are two main reasons for such slight differences. Firstly, the values from our previous study on the $\text{He}_N\text{-Rb}_2$ system were obtained by averaging from the plateau region observed for $E = E(M)$, and secondly the present results do not include a $3k_B T$ contribution which was erroneously accounted for in that work.

Differences between the quantum and the non-rotating Rb_2 total energies exhibit a dependence with the number of helium atoms of the cluster. According to Table 1 at $T = 1$ K such a difference increases from $\sim 5 \text{ cm}^{-1}$ for $N = 20$ to $\sim 12 \text{ cm}^{-1}$ for $N = 40$. For $\text{He}_{40}\text{Rb}_2$ there is some extra 3 cm^{-1} variation between both treatments when T is increased to 2 K. At this temperature, the cluster formed by Rb_2 attached to 20 helium atoms becomes unstable, with a positive energy, a result which was also found for the non-rotating system [22]. The positive contribution in the quantum Rb_2 cluster comes, as expected, from two sources, the rotational energy, strictly zero in the fixed impurity calculation, and the kinetic energy contribution due to the translational movement which is not restricted in this approach. In this sense it is found that the translational contribution of the Rb_2 kinetic energy

term accounts for $\sim 3 \text{ cm}^{-1}$ and 6 cm^{-1} at $T = 1$ K when the impurity is attached to 20 and 40 helium atoms respectively, but it increases up to $\sim 11 \text{ cm}^{-1}$ for $\text{He}_{40}\text{Rb}_2$ at $T = 2$ K. The quantum treatment of the Rb_2 impurity, taking into account the rotational and translational degrees of freedom, leads to variations in the energy with respect to the fixed impurity which are noticeably smaller in comparison with the findings of a similar comparative study performed for helium clusters doped with OCS [7]. In that case, for the temperature under consideration, $T = 0.37$ K, the energy of the $\text{He}_{64}\text{-OCS}$ cluster differs $\sim 20 \text{ cm}^{-1}$ depending on the approach chosen in the PIMC calculation.

The stability of the doped clusters He_NRb_2 is analyzed in terms of the energies of the corresponding pure He_N droplets. Whereas at $T = 2$ K, energies for $E(\text{He}_{20})$ and $E(\text{He}_{40})$ are both positive, as reported in Ref. [54], at $T = 1$ K, values of $-9.41 \pm 4.50 \text{ cm}^{-1}$ and $-47.45 \pm 11 \text{ cm}^{-1}$ for $N = 20$ and 40 are obtained respectively. Therefore, it is then possible to conclude that the doped clusters formed attaching Rb_2 to He_{20} and He_{40} , are stable with respect to the corresponding pure He clusters. A more subtle issue however regards the case of $\text{He}_{40}\text{Rb}_2$ at $T = 2$ K, where the error bar [55,56] (not shown in Table 1 but of the same order as in our previous fixed-impurity PIMC calculation [22]) becomes remarkably large, and consequently may invade positive energy region. In addition calculations performed with a much more relaxed confinement restrictions, with an enlargement of 3 Å and 2 Å in the admitted $\text{He-Rb}_2(\text{CM})$ and $\text{He-He}_N(\text{CM})$ distances respectively, yield to positive values for the binding energy of such a cluster.

In order to estimate the difference of the isolated (vacuum) Rb_2 rotation with respect to the situation inside the $\text{He}_N\text{-Rb}_2$ cluster under study we have followed a similar approach as Guillon *et al.* [21] in their mean field treatment. It is possible to calculate the contribution coming from the in-plane rotation (see Eq. (7) of Ref. [21]), by means of a Boltzmann average. This calculation leads to approximately 0.7 cm^{-1} at $T = 1$ K, which means that if the total rotational energy is about 1.24 cm^{-1} for both $N = 20$ and 40 He atoms (Table 1), the out-of-plane contribution (hindered rotation) due to the presence of the surrounding He atoms accounts for about 0.5 cm^{-1} . A similar analysis at $T = 2$ K reveals on the contrary that most of the rotational energy comes from the in-plane rotation, thus suggesting a negligible effect coming from the He environment. This feature is consistent with the uncertainty of the stability of the doped clusters at such temperature discussed in the previous paragraph.

Quantum Rb ₂	<i>N</i>	<i>V</i>	<i>E_{kin}</i>	<i>E_{rot}</i>	<i>E</i>
<i>T</i> = 1 K	20	-81.51	70.03	1.24	-10.32
	40	-252.99	201.23	1.24	-50.52
<i>T</i> = 2 K	40	-197.13	195.37	1.39	-0.37

Fixed Rb ₂	<i>N</i>	<i>V</i>	<i>E_{kin}</i>	<i>E_{rot}</i>	<i>E</i>
<i>T</i> = 1 K	20	-81.96	66.88	-	-15.08
	40	-257.68	194.82	-	-62.86
<i>T</i> = 2 K	40	-202.10	186.56	-	-15.54

Table 1. Potential (*V*), kinetic translational (*E_{kin}*), rotational (*E_{rot}*) and total energy (*E*) for quantum and classical simulation of rubidium dimer. Units are cm⁻¹.

4.2 Distributions

The structure of the doped clusters with rotating quantum Rb₂ is further analyzed through its probability density distributions. In particular, in Fig. 3 we present the distributions of the He atoms with respect to the impurity $\rho_{\text{He}}(z, r)$ in the frame defined by the CM of Rb₂ for *N* = 20 and *N* = 40 at *T* = 1 K: *z* is the molecular axis of the rubidium diatom and *r* is the distance from that *z*-axis. The distribution for He₂₀Rb₂ exhibits a broad maximum peak around ~ 12 Å which becomes slightly less pronounced when the number of helium atoms is increased up to 40. In both cases the resulting distributions display a much less structured profile than that exhibited by earlier results for He_N-OCS [7]. One of the main differences between these two doped systems regards the location of the impurity with respect to the helium environment: whereas OCS becomes completely solvated by the helium atoms, Rb₂ remains at the surface of the nanodroplet. A feature which could also explain the variations observed on the energies of the clusters He_NOCS depending on whether or not the impurity is assumed to be fixed.

An indication of the external location of the dopant in the case of the title aggregates comes from the comparison with the fixed Rb₂ calculation. The classical treatment, which was found to predict a non-solvating structure for the cluster [22], leads to similar density distributions. As shown in Fig. 4 the main differences between the quantum and the classical approaches are the extension of the distributions, but the broad maximum peaks observed in Fig. 3 are also evident.

The distributions for the He-Rb₂(CM) distance are shown in Fig. 5 for the He₂₀-Rb₂ and He₄₀-Rb₂ clusters at *T* = 1 K. The comparison between the two doped droplets reveals that the helium atoms stay at slightly larger distances with respect to the CM of the impurity. This finding is then consistent with the much less pronounced maximum peaks seen in Fig. 4.

It is worth mentioning that similar density distributions for *T* = 2 K are more spatially extended, thus covering a great deal of the distance allowed by the confinement restrictions. In fact, as already discussed about the apparent lack of stability of the He₄₀-Rb₂ cluster at this temperature, in cases where such limitations are somehow relaxed the obtained distributions reveal the tendency of the helium atoms to abandon the droplet.

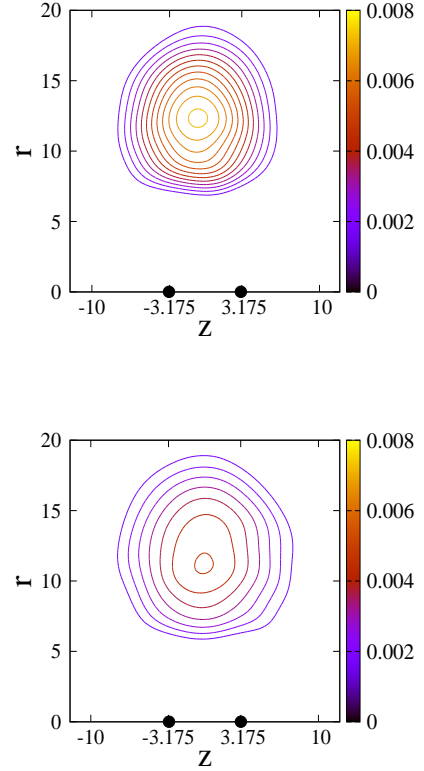


Fig. 3. $\rho_{\text{He}}(z, r)$ density distributions obtained by means of the quantum Rb₂ PIMC calculation for *N* = 20 (upper panel) and *N* = 40 (lower panel) at *T* = 1 K. Black points in *z* axis indicate rubidium atom positions. Units for *r* and *z* are Å.

Finally, we analyse angular density distributions, shown in Fig. 6, for both θ , the angle formed between the position vector for a He atom and the Rb₂ molecular axis, and γ , the angle formed by any pair of He atoms and the CM of the Rb₂ for the cluster with *N* = 40 and *T* = 1 K. The obtained distributions are in perfect consistence with those for the fixed Rb₂ PIMC calculation (see Figs. 4 and 7 of Ref. [22]), thus indicating that the consideration of the rotational and translational degrees of freedom of Rb₂ does not introduce significant changes from the non-rotating case in the overall structure of the cluster. In our previous study, the observed preference in the γ distribution along $\cos\gamma \sim 1$, was interpreted as indication of a packed structure of the helium atoms which thereby push the Rb₂ impurity outside.

This agreement with the overall features observed for the fixed Rb₂ doped cluster is consistent with similar comparisons established before for some other systems such as He_N-OCS [7].

5 Conclusions

In this work we have performed finite temperature PIMC calculations of physical properties for a rigid-rotating Rb₂

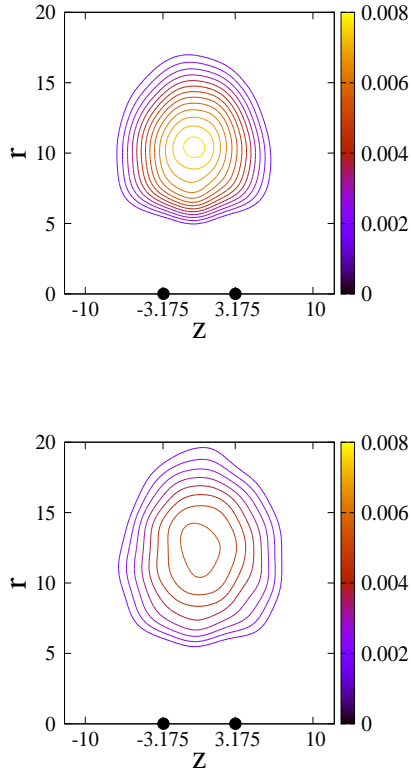


Fig. 4. Same as Fig. 3 for the fixed Rb_2 calculation.

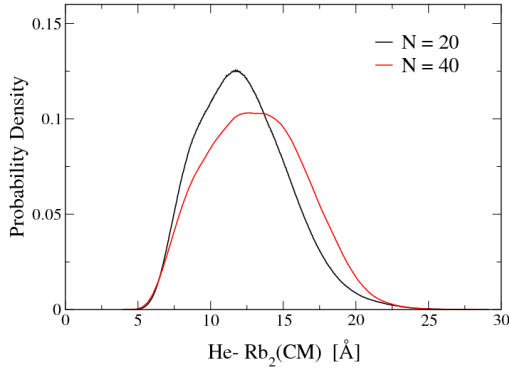


Fig. 5. One-particle radial distributions for $N = 20$ and $N = 40$ at $T = 1$ K.

dimer attached in a $^4\text{He}_N$ droplet ($N = 20$ and $N = 40$) at $T = 1$ and 2 K. The assumption of an infinite mass of Rb_2 molecule ($m_{\text{He}}/m_{\text{imp}} \approx 0.02$) and a fixed position in the overall cluster for the considered impurity in bosonic helium environment does not account for quantum effects which are not negligible due to the proximity of the system to instability regions caused by the weak interactions in play. Although there exist differences in the energies for the systems under study, the overall features regarding the structure of the doped $\text{He}_N\text{-Rb}_2$ clusters are seen

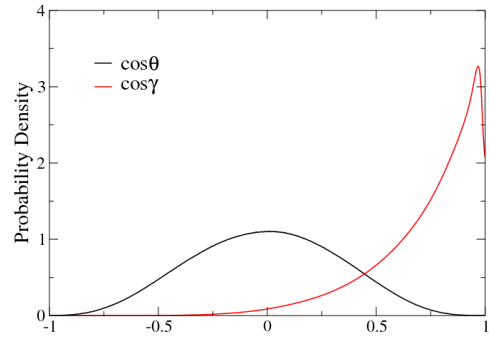


Fig. 6. One-particle (black) and two-particle (red) angular distributions for $N = 40$ at $T = 1$ K.

not to vary dramatically, thus confirming the physical consequences of the particularly weak nature of the dopant's interactions with the He droplets.

Acknowledgments

The authors would like to thank Centro de Cálculo (IFF, CSIC) and Centro Técnico de Informática (CTI, CSIC) for the allocation of computer time. This work has been supported by MICINN, Grant No. FIS2011-29596-CO2-01. R. R.-C. acknowledges the Spanish programs JAE-PREDOC grant No. JAE-Pre-2010-01277.

References

1. F. Paesani, K.B. Whaley, *J. Chem. Phys.* **121**, 5293 (2004)
2. N. Blinov, P.N. Roy, *J. Low Temp. Phys.* **140**, 253 (2005)
3. L. Wang, D. Xie, H. Guo, H. Li, R.J.L. Roy, P.N. Roy, *J. Mol. Spectrosc.* **267**, 136 (2011)
4. L. Wang, D. Xie, R.J.L. Roy, P.N. Roy, *J. Chem. Phys.* **137**, 104311 (2012)
5. R.E. Zillich, F. Paesani, Y. Kwon, K.B. Whaley, *J. Chem. Phys.* **123**, 114301 (2005)
6. W. Topic, W. Jäger, N. Blinov, P. Roy, M. Botti, S. Moroni, *J. Chem. Phys.* **125**, 144310 (2006)
7. S. Miura, *J. Chem. Phys.* **126**, 114308 (2007)
8. S. Miura, *J. Chem. Phys.* **126**, 114309 (2007)
9. Z. Li, L. Wang, H. Ran, D. Xie, N. Blinov, P.N. Roy, H. Guo, *J. Chem. Phys.* **128**, 224513 (2008)
10. C. Ing, K. Hinsien, J. Yang, T. Zeng, H. Li, P.N. Roy, *J. Chem. Phys.* **136**, 224309 (2012)
11. E. Bodo, F. Sebastianelli, F.A. Gianturco, E. Yurtsever, M. Yurtsever, *J. Chem. Phys.* **120**, 9160 (2004)
12. E. Bodo, F. Gianturco, E. Yurtsever, *J. Low Temp. Phys.* **138**, 259 (2005)
13. S. Bovino, E. Coccia, E. Bodo, D. Lopez-Durán, F.A. Gianturco, *J. Chem. Phys.* **130**, 224903 (2009)
14. D. López-Durán, R. Pérez de Tudela, R. Rodríguez-Cantano, T. González-Lezana, M.P. de Lara-Castells, G. Delgado-Barrio, P. Villarreal, *Phys. Scr.* **84**, 028107 (2011)

15. R. Rodríguez-Cantano, D. López-Durán, T. González-Lezana, G. Delgado-Barrio, P. Villarreal, E. Yurtsever, F.A. Gianturco, *J. Phys. Chem. A* **116**, 2394 (2012)
16. S. Bovino, E. Bodo, E. Yurtsever, F.A. Gianturco, *J. Chem. Phys.* **128**, 224312 (2008)
17. B. Grüner, M. Schlesinger, P. Heister, W.T. Strunz, F. Stienkemeier, M. Mudrich, *Phys. Chem. Chem. Phys.* **13**, 6816 (2011)
18. D. Caruso, M. Tacconi, E. Yurtsever, S. Bovino, F. Gianturco, *Eur. Phys. J. D* **65**, 167 (2011)
19. M. Schlesinger, W.T. Strunz, *New J. Phys.* **14**, 013029 (2012)
20. R. Pérez de Tudela, M. Márquez-Mijares, T. González-Lezana, O. Roncero, S. Miret-Artés, G. Delgado-Barrio, P. Villarreal, *J. Chem. Phys.* **132**, 244303 (2010)
21. G. Guillon, A. Zanchet, M. Leino, A. Viel, R.E. Zillich, *J. Phys. Chem. A* **115**, 6918 (2011)
22. R. Rodríguez-Cantano, D. López-Durán, R. Pérez de Tudela, T. González-Lezana, G. Delgado-Barrio, P. Villarreal, F. Gianturco, *Comp. Theor. Chem.* **990**, 106 (2012)
23. F. Ancilotto, G. DeToffol, F. Toigo, *Phys. Rev. B* **52**, 16125 (1995)
24. P.B. Lerner, M.W. Cole, E. Cheng, *J. Low Temp. Phys.* **100**, 501 (1995)
25. F. Stienkemeier, J. Higgins, W.E. Ernst, G. Scoles, *Phys. Rev. Lett.* **74**, 3592 (1995)
26. F. Stienkemeier, W.E. Ernst, J. Higgins, G. Scoles, *J. Chem. Phys.* **102**, 615 (1995)
27. J. Higgins, C. Callegari, J. Reho, F. Stienkemeier, W.E. Ernst, M. Gutowski, G. Scoles, *J. Phys. Chem. A* **102**, 4952 (1998)
28. J.H. Reho, J.P. Higgins, K.K. Lehmann, *Faraday Discuss.* **118**, 33 (2000)
29. P. Claas, G. Droppelmann, C.P. Schulz, M. Mudrich, F. Stienkemeier, *J. Phys. B: At., Mol. Opt. Phys.* **39**, 1151 (2006)
30. O. Bünermann, F. Stienkemeier, *Eur. Phys. J. D* **61**, 645 (2011)
31. Y. Kwon, D.M. Ceperley, K.B. Whaley, *J. Chem. Phys.* **104**, 2341 (1996)
32. N. Blinov, X. Song, P.N. Roy, *J. Chem. Phys.* **120**, 5916 (2004)
33. R. Pérez de Tudela, D. López-Durán, T. González-Lezana, G. Delgado-Barrio, P. Villarreal, F.A. Gianturco, E. Yurtsever, *J. Phys. Chem. A* **115**, 6892 (2011)
34. M.H. Müser, *Mol. Simul.* **17**, 131 (1996)
35. E.G. Noya, L.M. Ses, R. Ramirez, C. McBride, M.M. Conde, C. Vega, *Mol. Phys.* **109**, 149 (2011)
36. G. Guillon, A. Zanchet, M. Leino, A. Viel, R.E. Zillich, *J. Phys. Chem. A* **115**, 6918 (2011)
37. D. López-Durán, R. Rodríguez-Cantano, T. González-Lezana, G. Delgado-Barrio, P. Villarreal, E. Yurtsever, F.A. Gianturco, *J. Phys.: Condens. Matter* **24**, 104014 (2012)
38. G. Guillon, A. Viel, J.M. Launay, *J. Chem. Phys.* **136**, 174307 (2012)
39. B. Bernu, D. Ceperley, *J. Phys. Chem. Solids* **66**, 1462 (2005)
40. D. Marx, M.H. Müser, *J. Phys.: Condens. Matter* **11**, 117 (1999)
41. Y.K. P. Huang, K.B. Whaley, *Microscopic Approaches to Quantum Liquids in Confined Geometries*, Vol. Series on Advances in Quantum Many-Body Theory (World Scientific, 2002), chapter 3. The Finite-temperature Path Integral Monte Carlo Method and Its Application to Superfluid Helium Clusters
42. E.G. Noya, C. Vega, C. McBride, *J. Chem. Phys.* **134**, 054117 (2011)
43. D.M. Ceperley, *Rev. Mod. Phys.* **67**, 279 (1995)
44. L. Brualla, K. Sakkos, J. Boronat, J. Casulleras, *J. Chem. Phys.* **121**, 636 (2004)
45. B.J. Berne, D. Thirumalai, *Annu. Rev. Phys. Chem.* **37**, 401 (1986)
46. R.E. Zillich, J.M. Mayrhofer, S.A. Chin, *J. Chem. Phys.* **132**, 044103 (2010)
47. K.R. Glaesemann, L.E. Fried, *J. Chem. Phys.* **116**, 5951 (2002)
48. M.F. Herman, E.J. Bruskin, B.J. Berne, *J. Chem. Phys.* **76**, 5150 (1982)
49. N. Metropolis, A.W. Rosenbluth, M.N. Rosenbluth, A.H. Teller, E. Teller, *J. Chem. Phys.* **21**, 1087 (1953)
50. C. McBride, C. Vega, E.G. Noya, R. Ramirez, L.M. Sese, *J. Chem. Phys.* **131**, 024506 (2009)
51. M. Sprik, M.L. Klein, D. Chandler, *Phys. Rev. B: Condens. Matter Mater. Phys.* **31**, 4234 (1985)
52. R.A. Aziz, M.J. Slaman, *J. Chem. Phys.* **94**, 8047 (1991)
53. M. Iwamatsu, *Comput. Phys. Commun.* **142**, 214 (2001)
54. J. Boronat, K. Sakkos, E. Sola, J. Casulleras, *J. Low Temp. Phys.* **148**, 845 (2007)
55. J. Cao, B.J. Berne, *J. Chem. Phys.* **91**, 6359 (1989)
56. H. Flyvbjerg, H.G. Petersen, *J. Chem. Phys.* **91**, 461 (1989)